

Three-dimensional Sandglass Magnet with Non-Kramers ions

Yan-Xing Yang,¹ Yao Wang,¹ Zhao-Feng Ding,¹ A. D. Hillier,² and Lei Shu^{1,3,4,*}

¹*State Key Laboratory of Surface Physics, Department of Physics, Fudan University, Shanghai 200438, China*

²*ISIS Facility, STFC Rutherford Appleton Laboratory, Chilton, Didcot, Oxfordshire, OX110QX, United Kingdom*

³*Collaborative Innovation Center of Advanced Microstructures, Nanjing 210093, China*

⁴*Shanghai Research Center for Quantum Sciences, Shanghai 201315, China*

(Dated: January 25, 2022)

We report the magnetic and thermodynamic properties of a newly synthesized fluorite oxide Tm_3SbO_7 , where two inequivalent sets of non-Kramers Tm^{3+} ions form a three-dimensional (3D) sandglass-type sublattice. X-ray diffraction and the Rietveld refinement confirm the space group $C222_1$, and site-mixing is not likely for this compound. Magnetic susceptibility and specific heat measurements exclude the existence of an ordered or a glassy state temperatures down to 0.1 K. The magnetic entropy shows a two-step release, indicating the two inequivalent Tm^{3+} ions are weakly correlated and play a part in different energy scales. The low-energy properties of Tm_3SbO_7 are dominated by the two lowest energy levels of Tm^{3+} with a finite energy gap, and the intrinsic transverse field Ising model with a quantum paramagnetic state can be applied to this 3D magnet. While the absence of magnetic order is further confirmed by the muon spin relaxation measurements, the dynamic property of the low-energy state is also revealed. Therefore Tm_3SbO_7 provides a new platform of studying quantum magnetism and dynamic properties.

I. INTRODUCTION

In quantum materials, the concept of emergent phenomena due to strong-correlations between electrons or magnetic moments, quantum entanglement, topology or frustration has attracted a lot of attention^{1,2}. Such a concept is widely applied in many interesting systems including high-temperature superconductor, topological insulator and quantum spin liquid (QSL). The last one, QSL, is a novel quantum system where the magnetic order is suppressed by quantum fluctuations even at zero temperature. Considerable efforts in searching for QSL have been seen since the concept was proposed by Anderson proposed in 1973³. Currently, QSL has become a hot topic in condensed matter physics due to its potential applications in quantum communication and computing⁴.

However, experimental identification of a QSL remains a great challenge since one can not reach absolute zero temperature to identify a specific material's ground state. A compromise is to measure the enough low-temperature properties by using a variety of methods, including magnetic susceptibility, specific heat, muon spin relaxation (μ SR), and nuclear magnetic resonance measurements to exclude the magnetic ordering or freezing^{5,6}. However, a material that does not order magnetically at low temperatures may be caused by structure or chemical component disorder^{7,8}, or is only simply due to a cooperative paramagnetic state^{9,10}. In addition to the absence of magnetic order, a recognized QSL material needs to satisfy several conditions including fractional excitations and long-range correlated dynamical spins. To demonstrate the existence of fractional excitations, the residual linear term in low-temperature specific heat^{11–14} and thermal conductivity^{12,15,16}, as well as the continuum magnetic excitation spectra in inelastic neutron scattering measurements^{17,18} are all expected. Besides, the low-temperature plateau of the muon spin relaxation rates is an evidence of persistent spin dynamics in an entangled spin system^{11,19,20}.

So far numerous two-dimensional QSL candidates have been reported, among which either geometry frustration^{21,22}

or Kitaev interactions^{4,23,24} introduces quantum fluctuations. However, promising three-dimensional (3D) QSL candidates are still rare since higher dimensionality suppresses the quantum fluctuations. Hyperkagome $Na_4Ir_3O_8$ ^{25–27} and pyrochlore $Pr_2Ir_2O_7$ ^{28–31} are two representative 3D QSL candidates and have been the subject of extensive studies.

We report a new 3D non-Kramers magnet Tm_3SbO_7 . The fluorite structure was determined by the X-ray diffraction (XRD) pattern. The absence of magnetic order as well as the persistent spin dynamics in a 3D system are evidenced by the magnetization, specific heat and μ SR measurements. Moreover, based on the crystal electric field (CEF) calculation and the specific heat results, we find that the low-energy properties of Tm_3SbO_7 are dominated by the two lowest energy levels of Tm^{3+} with a finite energy gap. The CEF splitting between the two lowest levels can be considered as an intrinsic transverse field. Considering the small exchange interactions between rare-earth, the current experimental observations can be described by the transverse field Ising model (TFIM)^{32–36}, with a quantum paramagnetic state. Although geometry frustration is not found based on the lattice structure, the frustration due to the competition of exchange interactions between the nearest-neighbor and the next-nearest-neighbor Tm^{3+} ions, is still possible. Due to the fact that only a polycrystalline sample is available currently, high quality of single crystal and more experiments are required to further identify the ground state of Tm_3SbO_7 .

II. EXPERIMENTS

Polycrystalline Tm_3SbO_7 and its non-magnetic analog Lu_3SbO_7 were prepared by the solid state reaction. Stoichiometric amounts of Sb_2O_3 and Ln_2O_3 ($Ln = Tm$ or Lu) were mixed and thoroughly ground and heated at 1500 °C for 7 days. Then polycrystalline samples were obtained after two additional re-grindings and heating. The single phase of the two samples was checked by powdered XRD measure-

ments using a Bruker D8 advanced X-ray diffraction spectrometer ($\lambda = 1.5418 \text{ \AA}$). The Rietveld refinement of XRD data was conducted using FullProf software. DC magnetic susceptibility measurements were carried out in the temperature range from 2 K to 300 K by using a Magnetic Property Measurement System (MPMS, Quantum Design). The measurements of AC magnetic susceptibility from 0.1 K to 4 K and specific heat from 0.1 K to 300 K were carried out in a Physical Property Measurement System (PPMS, Quantum Design) equipped with dilution refrigerator. μSR measurements with temperatures from 0.07 K to 43 K and longitudinal external magnetic fields up to 0.3 T were performed on the MuSR spectrometer at ISIS Neutron and Muon Facility, STFC, Rutherford Appleton Laboratory, UK.

III. RESULTS

A. Crystal structure

The fluorite-related structure has been reported in the rare earth rhenium oxides $Ln_3\text{ReO}_7$ ($Ln = \text{Y, Er-Lu}$)³⁷ and the authors found that $Ln_3\text{ReO}_7$ (for $Ln = \text{Y, Er, Tm}$) have the orthorhombic structure with space group $C222_1$ while $Ln_3\text{ReO}_7$ (for $Ln = \text{Yb, Lu}$) have the cubic structure with space group $Fm\bar{3}m$. The XRD pattern of Tm_3SbO_7 is shown in Fig. 1(a). In the process of resolving the structure of this new material, we have firstly tried the space group $Fm\bar{3}m$ with Tm and Sb atoms randomly occupying the 4a Wyckoff position, and oxygen atoms occupying the 4b position. Only a few obvious strong reflections are eligible and these remaining weak reflections point out that the symmetry is lower than cubic structure. As a result, the orthorhombic structure with space group $C222_1$ was used, and it matches the XRD data exactly, indicating the site-mixing is not likely. The Rietveld refinement results are shown in TABLE I.

The unit cell of Tm_3SbO_7 is shown in Fig. 1(b). There are two different Tm sites in Tm_3SbO_7 with the ratio of Tm1:Tm2 = 2:1. As shown in Figs. 1(c-d), Tm1 atoms form the twisted grids which are parallel to the (010) plane. Tm2 and Sb atoms residing in between Tm1 grids form the one-dimensional chains parallel to the [001] direction, respectively. All the Tm atoms construct the edge-shared sandglass-type structure. The bond lengths of these neighboring Tm atoms vary in a small range from 3.53 \AA to 3.87 \AA , indicating Tm_3SbO_7 is a 3D magnet.

B. Magnetic susceptibility

Dc-magnetic susceptibility χ_{dc} of Tm_3SbO_7 measured under a magnetic field of 0.5 T from 2 K to 300 K are shown in Fig. 2. At high temperatures, χ_{dc} increases as the temperature is reduced. Temperature dependence of the data between 100 and 300 K gives the Curie-Weiss temperature $\Theta_{\text{CW}} = -23.3 \text{ K}$ and the effective magnetic moment $\mu_{\text{eff}} = 7.53 \mu_{\text{B}}$. The negative value of Θ_{CW} indicates the antiferromagnetic interactions between Tm^{3+} magnetic moments. $\mu_{\text{eff}} = 7.53 \mu_{\text{B}}$

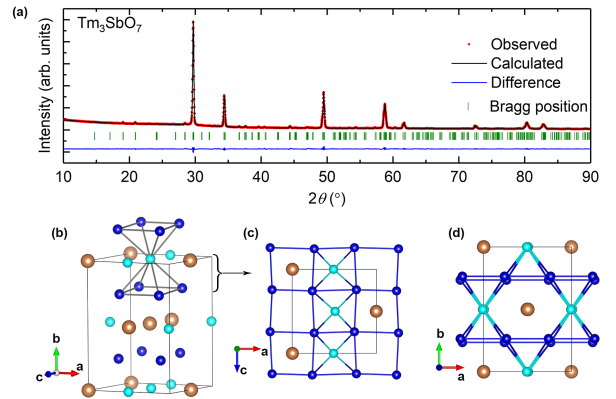


FIG. 1. (a) Rietveld refinement of powder XRD pattern of Tm_3SbO_7 at room temperature using the orthorhombic structure with space group $C222_1$. The red dots, black line, and blue line are the experimental data, the calculated patterns, and the differences, respectively. The green bars indicates the Bragg reflections. (b) The unit cell of Tm_3SbO_7 as well as the Schematic diagram of the sandglass-type configuration of Tm^{3+} ions. Dark blue: Tm1; light blue: Tm2; brown: Sb. (c) Top view of two selected layers of the unit cell. (d) Front view of the unit cell.

TABLE I. Rietveld refinement results for Lu_3SbO_7 . $R_{wp} = 2.39\%$, $R_p = 3.73\%$, $\chi^2 = 11.9$; $a = 7.389 \text{ \AA}$, $b = 10.398 \text{ \AA}$, $c = 7.361 \text{ \AA}$; $\alpha = \beta = \gamma = 90^\circ$; Space Group: $C222_1$.

Wyckoff						
Atom positions	x	y	z	$B/\text{\AA}^2$	Occ.	
Tm1	8c	0.2424(8)	0.2352(9)	0.7431(6)	0.1587(6)	1
Tm2	4a	0.0094(1)	0.5	0.5	0.1598(7)	1
Sb	4a	0.0129(8)	0	0	0.0551(5)	1
O1	8c	0.2165(0)	0.1351(4)	0.4982(9)	0	1
O2	8c	0.2157(8)	0.1166(8)	0.0697(4)	4.7098(3)	1
O3	4b	0	0.0840(5)	0.75	1.8571(2)	1
O4	4b	0	0.3557(9)	0.75	0.0822(5)	1
O6	4b	0	0.3640(6)	0.25	0.5970	1

is close to the theoretical value $\mu_{\text{calc}} = 7.57 \mu_{\text{B}}$ for Tm^{3+} ions with the spin-orbital coupling ground state $^3\text{H}_6$. The crystal electric field (CEF) splitting of the 13-fold degenerate energy level of Tm^{3+} was calculated using PyCrystalField³⁸, a Python software based on point charge approximation and the schematic of CEF splitting of Tm1 is shown in the inset of Fig. 2. For Tm1, the ground state and the first excited state form a non-degenerate doublet and the energy splitting gap h between the two states is 0.25 meV, which is much smaller than Δ (≈ 29 meV), the energy gap to the other higher excited states. So the doublet is regarded as an effective spin- $\frac{1}{2}$ local moment and governs the low-temperature properties. For Tm2, the calculated energy levels from low to high are 0 meV, 0.91 meV, 3.79 meV, 6.53 meV, 7.68 meV, 10.89 meV, 28.12 meV, ..., where the lowest 6 levels are gapped by a relatively large gap Δ (≈ 17 meV) from other levels. More details about the energy levels of Tm^{3+} ions are introduced in Sec. III C.

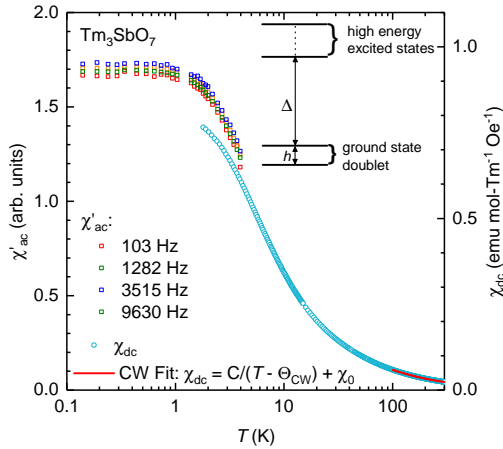


FIG. 2. Temperature dependence of dc magnetic susceptibility χ_{dc} (circles) and the real part of ac susceptibility χ'_{ac} (squares). χ_{ac} was measured in zero static field with a driven field of 1 Oe from 0.1 K to 4 K. χ_{dc} was measured under $\mu_0 H=0.5$ T from 2 K to 300 K. χ_{dc} between 100-300 K was fitted using Curie-Weiss law as shown in the picture. The temperature-independent χ_0 is induced by Van-Vleck susceptibility. Inset: schematic of the CEF splitting of Tm1 in Tm_3SbO_7 .

When the temperature is cooled down below 100 K, χ_{dc} slowly deviates from the Curie-Weiss law and tends to become flat at low temperatures. No peak reflecting phase transition or separation between zero-field cooling and field cooling (not shown) is found down to 2 K in the DC magnetic susceptibility measurements. Moreover, AC susceptibility was measured from 4 K to 0.1 K. χ'_{ac} data with different driving frequencies show similar behavior, gradually increases with lowering the temperature and finally saturates below 1 K without showing any anomalies. Combining these two methods, magnetic ordered state as well as the spin glass state in Tm_3SbO_7 can be ruled out.

C. Specific heat

To further investigate the thermodynamics of Tm_3SbO_7 , we measured the specific heat down to about 0.1 K by applying various magnetic fields, as shown in Fig. 3(a). We subtract the phonon contribution, which is obtained from nonmagnetic oxide Lu_3SbO_7 and depicted (black points) in the inset of Fig. 3(a), from the total specific heat C_{total}/T of Tm_3SbO_7 . Due to the uncertainty of subtraction at high temperatures, the magnetic specific heat are only exhibited below the temperature of 120 K. The whole curve of C_M/T shows two overlapped broad bumps. However, there are no peaks associated with phase transition at such a wild temperature range, consistent with the magnetic susceptibility and μSR results.

We calculated the entropy increasing by integrating the C_M/T curve, as revealed in Fig. 3(b). The entropy can be roughly separated into 2 parts, $S_{M,1}$ and $S_{M,2}$ at lower and higher temperature respectively. Each of them contributes

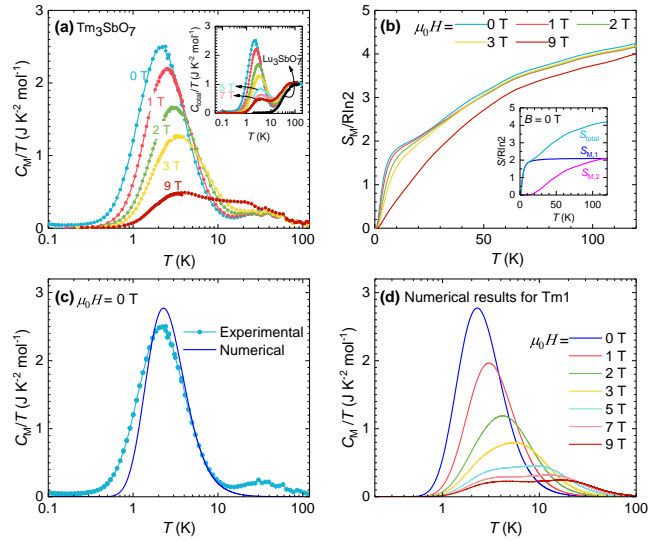


FIG. 3. (a) Temperature dependence of magnetic specific heat coefficient C_M/T of Tm_3SbO_7 . Inset: Temperature dependence of measured total specific heat coefficient C_{total}/T of Tm_3SbO_7 (colored scatters) and of non-magnetic analog Lu_3SbO_7 (black points). (b) Temperature dependence of magnetic entropy S_M obtained by integrating C_M/T from about $T = 0.1$ K to T . Inset: Two step entropy increasing under zero magnetic field. (c) Comparison between experimental results and numerical results of C_M/T for Tm1 under zero magnetic field. (d) Numerical results of C_M/T for Tm1 under different magnetic fields.

$2R\ln 2$ to the entropy increasing for per mole Tm_3SbO_7 .

A close-up of magnetic specific heat coefficient C_M/T measure at zero-field is shown in Fig. 3(c), depicted by dotted light-blue line. Based on the CEF calculation within point charge approximation, we find that two non-degenerate lowest energy levels of Tm1 at 8c Wyckoff position have a large energy gap, $\Delta = 28$ meV. Two Tm1 in each unit cell can offer $2R\ln 2$ entropy increasing, which is exactly the saturation value of $S_{M,1}$. Besides, the maximum of the lower-temperature bump of magnetic specific heat is about $0.4 k_B$ per Tm^{3+} (not shown here), consistent with the typical maximum of a Schottky anomaly.

From CEF calculation using the point charge model, for Tm2 at 4a Wyckoff position, there are 6 energy levels below a large energy gap and evenly distributed between 0-11 meV. This is consistent with the small bump at higher temperatures. As shown in the inset of Fig. 3(b), $S_{M,2}$ rising from 10 K reaches $R\ln 4$, and does not saturate around 120 K, the highest temperature we measured. It is reasonable that only 4 energy levels due to Tm2 at 4a Wyckoff position are covered below 120 K, $S_{M,2}$ will continue to increase above 120 K and saturate at $R\ln 6$. However, C_M/T is difficult to obtain due to the uncertainty of phonon subtraction at high temperatures.

As displayed in Fig. 3(a), by increasing the external magnetic fields, the lower-temperature bump is lowered and broadened, and the peak position moves to higher temperatures until $\mu_0 H = 5$ T. We give numerical calculation of C_M/T

due to Tm1 energy levels, as shown in Fig. 3(d). The details of the calculation is introduced in the Sec. IV C. The position of the higher-temperature bump does not move but gets broader with increasing applied magnetic fields, and there is no obvious bump at $\mu_0 H = 9$ T. Since the entropy under various magnetic fields have a roughly $4R\ln 2$ in total for per mole sample except for a small deficiency at the highest field we measured, we believe that $\mu_0 H = 9$ T magnetic field does not change the energy levels below 120 K.

D. μ SR

μ SR is a low-frequency probe of spin dynamics and is particularly sensitive to slow spin fluctuations³⁹, it is therefore ideally suited to studies of long-lived spin correlations in novel spin systems. We continue to study the intrinsic magnetic properties of Tm_3SbO_7 by performing μ SR experiments. Both the zero-field (ZF)- and longitudinal-field (LF)- μ SR spectra are shown in Fig. 4(a). The ZF- μ SR asymmetries are well fitted by a sum of two damped Kubo-Toyabe functions originating from two inequivalent muon sites:

$$A(t) = A_0 f_1 e^{-\lambda_1 t} G_z^{\text{KT}}(\delta_1, t) + A_0 (1 - f_1) e^{-\lambda_2 t} G_z^{\text{KT}}(\delta_2, t) \quad (1)$$

where A_0 is the initial asymmetry and f_1 represents the fraction of the first muon sites in sample. During the data processing, A_0 and f_1 were found to be temperature independent and therefore are fixed at the average values of 0.22 and 0.5, respectively. The exponential rates $\lambda_{1,2}$ are the muon spin relaxation rates usually related to the dynamic internal magnetic fields. $G_z^{\text{KT}}(\delta, t)$ is the well-known Kubo-Tayabe function in which the relaxation rates $\delta_{1,2}$ originate from static internal magnetic fields such as nuclear dipolar fields³⁹. As shown in Fig. 4(b) and (c), muons at two different stopping sites sense the same internal magnetic fields and the only difference is the strength. This indicates two muon sites are reasonable and the phase separation can be excluded.

Cooling from high temperatures, the dynamical relaxation rate $\lambda_{1,2}$ gradually goes up and shows broad peaks around 3 K and finally saturate below 1 K. The low-temperature plateau of muon relaxation rates is a sign of persistent spin dynamics^{11,19,20}. The dynamical property of internal fields is further confirmed by the LF- μ SR results (see Fig. 4(a)), since the muon depolarization will be completely decoupled under such an external longitudinal field if the internal fields are static or quasi-static. Note that although λ_2 is ten times smaller than λ_1 , both λ_1 and λ_2 show two peaks around the same temperatures. The two peaks of $\lambda_{1,2}$ are also consistent with the two bumps discovered in the specific heat measurements.

As shown in Fig. 4(c), the static muon spin relaxation rates $\delta_{1,2}$, similar to χ_{dc} and χ'_{ac} , increases with decreasing temperature and saturates below 1 K. We argue that the temperature-dependent $\delta_{1,2}$ are related to hyperfine-enhanced Tm nuclear moments⁴⁰. The enhanced value of the static Tm nuclear contribution, δ , has the formula:

$$\delta = (1 + k)\delta_0 \quad (2)$$

where δ_0 is the un-enhanced value of the static Tm nuclear contribution. $k = a_{4f}\chi_{\text{mol}}$ is the enhancement factor, where a_{4f} is the atomic hyperfine coupling constant and χ_{mol} is the DC magnetic susceptibility. Replace k in Eq. (2) with $a_{4f}\chi_{\text{mol}}$, we obtain $d\delta/d\chi_{\text{mol}} = a_{4f}\delta_0$, indicating that δ should be proportional to χ_{mol} with temperature as an implicit parameter. This is consistent with our experimental results as shown in Fig. 4(d). $\delta_{1,2}$ is proportional to χ_{dc} in a wide temperature range.

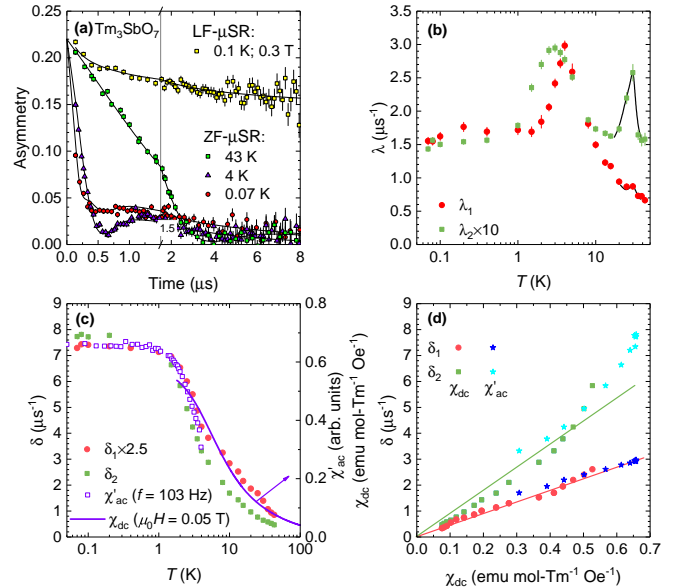


FIG. 4. (a) Representative μ SR asymmetry spectra (a constant background is subtracted) measured in ZF and LF. Solid lines are fits to the data. (b) Temperature dependence of ZF dynamic relaxation rate λ . The black line is to guide the eyes. (c) Temperature dependence of ZF static relaxation rate δ_1 (red dots) and δ_2 (green dots) at two different muon stopping sites. Purple line: dc-magnetic susceptibility χ_{dc} . Purple circle: ac-magnetic susceptibility χ'_{ac} , data from Fig. 2 and scaled with χ_{dc} . (d) Dependence of static relaxation rate $\delta_{1,2}$ of χ_{dc} or χ'_{ac} with temperature as an implicit parameter.

IV. DISCUSSION

A. Transverse field Ising model

To explain the experimental observations, TFIM, which is a well-studied theoretical model that has been successfully applied in many real materials^{32,34,36,41}, is introduced. In such a model, the ground state is quantum paramagnetic when the effect of transverse field is stronger than the exchange interactions between correlated spins. For Tm_3SbO_7 , two sets of inequivalent Tm^{3+} ions bring some difficulties to the analyses. Fortunately, based on the specific heat results, we find that Tm1 and Tm2 are only weakly correlated and the two lowest energy levels of Tm1 dominate the low-temperature properties. In such a case, we can reduce the problem to a 3D

TFIM in a twisted cuboid lattice occupied by Tm1 atoms, as described by the Hamiltonian:

$$H = \sum_{ij} J_{ij} S_i^z S_j^z - \sum_i h S_i^x \quad (3)$$

where J_{ij} is the exchange interaction, and h is the energy splitting between the two lowest energy levels of Tm1 ions, acting as the intrinsic transverse field. The competition between J_{ij} and h leads to different ground states. If J_{ij} is dominant, the ground state should be magnetically ordered, while if h is dominant, the ground state is quantum paramagnetic. Obviously, the second case is consistent with our current experimental data.

According to the position of the lower-temperature bump's maximum of C_M , we evaluated the energy splitting h between the two lowest levels. The value is about 7.4 K, whose order of magnitude is agreeable with the result estimated from point charge model of CEF. The numerical Schottky anomaly curve are plotted as dark-blue line in Fig. 3(c). The experimental data is roughly consistent with the Schottky characteristics except a slightly inconsistency at the left of the bump which is attributed to smaller temperature as denominators.

Based on the analysis above, we believe Tm_3SbO_7 maintains paramagnetic even cooling down to 0.1 K where the system stays at the lowest energy level states. Comparing the Curie-Weiss temperature $\Theta_{\text{CW}} = -23.3$ K with the large energy gap Δ , we believe the higher energy level has been gapped out before exchange interactions play a part during cooling down the system.

B. Dynamical muon spin relaxation rate, specific heat, and magnetic susceptibility

If we compare the temperature dependence of C_M/T with the dynamical muon relaxation rate λ , we find that the specific-heat bump is consistent with the relaxation rate peak. When $T \ll h$, the Tm electrons tend to stay in the lowest level and the transition probability between different levels is low. When T is close to h , the probability gets sufficient and hence leads to a maximum in C_M . When $T \gg h$, the probability drops again because different levels are almost equally occupied. The temperature dependence of electron transitions explains the change in specific heat. Meanwhile, since Tm^{3+} ions are magnetic, the electron transitions sensed by muons are considered as magnetic fluctuations. This is why the two different methods possess some common features in the temperature dependence.

The low-temperature plateau of λ is a sign of persistent spin dynamics. When cooling the temperature across $T_c = 1$ K, Tm_3SbO_7 evolves into quantum paramagnetic phase. Coincidentally, besides λ , both χ'_{ac} and χ_{dc} ($\propto \delta$) also saturate under 1 K. The fine uniformity indicates what we observed are all intrinsic. Moreover, since within a cuboid lattice it is hard to generate geometrical frustration, we speculate that the perturbation from Tm2 plays an important role and brings about the dynamics.

C. Simulation of specific heat data

Next, we simulate the evolution of the lower-temperature bump of C_M in a magnetic field. As we have mentioned, the crystal electric field at every single site plays an essential role instead of exchange interactions, thus we build a two-level system with an external field:

$$H = \frac{1}{2}h \begin{pmatrix} 0 & 1 \\ 1 & 0 \end{pmatrix} + \mu B_0 \cos \theta \begin{pmatrix} 1 & 0 \\ 0 & -1 \end{pmatrix} \quad (4)$$

where $h = 7.4$ K as we determined earlier, $\mu = 7.53 \mu_B \approx 5.058 \text{ K/T}$ measured from the magnetic susceptibility experiments. θ is the angle between the easy axis direction of Tm^{3+} and the external magnetic field with an amplitude B_0 . Because the sample is polycrystalline, we assume θ uniformly distributed in $[0, \pi]$.

To calculate the specific heat, we calculate the ensemble (temperature) average firstly, and then average over 10^5 samples with random angle θ . The numerical results are consistent with the lower-temperature bump of C_M/T with different external magnetic fields. As shown in Fig. 3(d), the higher the external field, the broader the Schottky bump. As for the suppression of height, we deem it is due to two reasons. Firstly, external field expands the energy difference between the two levels. This will drive the C_M bump to higher temperature and thus suppress the maximum of C_M/T . Secondly, the easy axis direction of Tm^{3+} ions in powder sample leads to different energy splitting. As a result, averaging all bumps with different maximum position give rise to a decreasing bump as the external field is increased.

Besides, from the point-charge-model's calculation of CEF, we also find the size of unit cell along c axis have a significant influence on the several lowest energy levels of Tm2. Even 0.1 Å can lead to a nearly degenerate doublet which offers a promising way to regulate the energy level and investigate how exchange interaction come into play in this system.

V. CONCLUSIONS

A new 3D Sandglass magnet Tm_3SbO_7 with non-Kramers ions has been discovered. We have carried out magnetic susceptibility, specific heat, and μSR experiments on polycrystalline samples. No long-range magnetic order and no signature of spin freezing were observed down to 0.07 K. Persistent spin dynamics are observed below 1 K and at least 3 kOe. The low-energy properties of Tm_3SbO_7 are dominated by the two lowest energy levels of Tm^{3+} with a finite energy gap, and the CEF splitting can be considered as an intrinsic transverse field. Thus the TFIM with a quantum paramagnetic state can be applied. However, the possibility that the absence of magnetic order due to the competition of exchange interactions between the nearest-neighbor and the next-nearest-neighbor Tm^{3+} ions, can not be completely excluded.

Tm_3SbO_7 provides a new platform for studying quantum magnetism and dynamic properties. To further identify the ground state of Tm_3SbO_7 , high-quality single crystals, careful

measurements of CEF splitting using inelastic neutron scattering are needed. Using pressure or element doping to regulate the energy splitting h can also be revealing.

ACKNOWLEDGMENTS

We thank Gang Chen, Yang Qi, Yuan Wan, and Jianda Wu for fruitful discussion. We are grateful to the ISIS cryogenics Group for their valuable help during the μ SR experiments (10.5286/ISIS.E.RB1820271). This research was funded by the National Natural Science Foundations of China, No. 12034004 and 12174065, and the Shanghai Municipal Science and Technology (Major Project Grant No. 2019SHZDZX01 and No. 20ZR1405300).

* leishu@fudan.edu.cn

- ¹ B. Keimer and J. E. Moore, *Nat. Phys.* **13**, 1045 (2017).
- ² Y. Tokura, M. Kawasaki, and N. Nagaosa, *Nat. Phys.* **13**, 1056 (2017).
- ³ P. W. Anderson, *Mater. Res. Bull.* **8**, 153 (1973).
- ⁴ A. Kitaev, *Annals of Physics* **321**, 2 (2006), january Special Issue.
- ⁵ C. Broholm, R. J. Cava, S. A. Kivelson, D. G. Nocera, M. R. Norman, and T. Senthil, “Quantum spin liquid,” (2020).
- ⁶ J. Wen, S.-L. Yu, S. Li, W. Yu, and J.-X. Li, *npj Quantum Mater.* **4**, 12 (2019).
- ⁷ I. Kimchi, J. P. Sheckelton, T. M. McQueen, and P. A. Lee, *Nat. Commun.* **9**, 4367 (2018).
- ⁸ I. Kimchi, A. Nahum, and T. Senthil, *Phys. Rev. X* **8**, 031028 (2018).
- ⁹ A. Keren, J. S. Gardner, G. Ehlers, A. Fukaya, E. Segal, and Y. J. Uemura, *Phys. Rev. Lett.* **92**, 107204 (2004).
- ¹⁰ B. G. Ueland, G. C. Lau, R. J. Cava, J. R. O’Brien, and P. Schiffer, *Phys. Rev. Lett.* **96**, 027216 (2006).
- ¹¹ Z.-F. Ding, Y.-X. Yang, J. Zhang, C. Tan, Z.-H. Zhu, G. Chen, and L. Shu, *Phys. Rev. B* **98**, 174404 (2018).
- ¹² J. M. Ni, B. L. Pan, B. Q. Song, Y. Y. Huang, J. Y. Zeng, Y. J. Yu, E. J. Cheng, L. S. Wang, D. Z. Dai, R. Kato, and S. Y. Li, *Phys. Rev. Lett.* **123**, 247204 (2019).
- ¹³ S. Yamashita, Y. Nakazawa, M. Oguni, Y. Oshima, H. Nojiri, Y. Shimizu, K. Miyagawa, and K. Kanoda, *Nat. Phys.* **4**, 459 (2008).
- ¹⁴ S. Yamashita, T. Yamamoto, Y. Nakazawa, M. Tamura, and R. Kato, *Nat. Commun.* **2**, 275 (2011).
- ¹⁵ M. Yamashita, N. Nakata, Y. Senshu, M. Nagata, M. Yamamoto Hiroshi, R. Kato, T. Shibauchi, and Y. Matsuda, *Science* **328**, 1246 (2010).
- ¹⁶ M. Yamashita, N. Nakata, Y. Kasahara, T. Sasaki, N. Yoneyama, N. Kobayashi, S. Fujimoto, T. Shibauchi, and Y. Matsuda, *Nat. Phys.* **5**, 44 (2008).
- ¹⁷ R. Coldea, D. A. Tennant, A. M. Tsvelik, and Z. Tylczynski, *Phys. Rev. Lett.* **86**, 1335 (2001).
- ¹⁸ A. Banerjee, J. Yan, J. Knolle, A. Bridges Craig, B. Stone Matthew, D. Lumsden Mark, G. Mandrus David, A. Tennant David, R. Moessner, and E. Nagler Stephen, *Science* **356**, 1055 (2017).
- ¹⁹ S. R. Dunsiger, A. A. Acczel, C. Arguello, H. Dabkowska, A. Dabkowski, M. H. Du, T. Goko, B. Javanparast, T. Lin, F. L. Ning, H. M. Noad, D. J. Singh, T. J. Williams, Y. J. Uemura, M. J. Gingras, and G. M. Luke, *Phys. Rev. Lett.* **107**, 207207 (2011).
- ²⁰ L. J. Chang, M. R. Lees, G. Balakrishnan, Y. J. Kao, and A. D. Hillier, *Sci. Rep.* **3**, 1881 (2013).
- ²¹ L. Balents, *Nature* **464**, 199 (2010).
- ²² Y. Zhou, K. Kanoda, and T.-K. Ng, *Rev. Mod. Phys.* **89**, 025003 (2017).
- ²³ K. Kitagawa, T. Takayama, Y. Matsumoto, A. Kato, R. Takano, Y. Kishimoto, S. Bette, R. Dinnebier, G. Jackeli, and H. Takagi, *Nature* **554**, 341 (2018).
- ²⁴ S. Pei, L.-L. Huang, G. Li, X. Chen, B. Xi, X. Wang, Y. Shi, D. Yu, C. Liu, L. Wang, F. Ye, M. Huang, and J.-W. Mei, *Phys. Rev. B* **101**, 201101 (2020).
- ²⁵ Y. Okamoto, M. Nohara, H. Aruga-Katori, and H. Takagi, *Phys. Rev. Lett.* **99**, 137207 (2007).
- ²⁶ G. Chen and L. Balents, *Phys. Rev. B* **78**, 094403 (2008).
- ²⁷ Y. Zhou, P. A. Lee, T.-K. Ng, and F.-C. Zhang, *Phys. Rev. Lett.* **101**, 197201 (2008).
- ²⁸ S. Nakatsuji, Y. Machida, Y. Maeno, T. Tayama, T. Sakakibara, J. Duijn, L. Balicas, J. N. Millican, R. T. Macaluso, and J. Y. Chan, *Phys. Rev. Lett.* **96**, 087204 (2006).
- ²⁹ G. Chen, *Phys. Rev. B* **94**, 205107 (2016).
- ³⁰ X.-P. Yao and G. Chen, *Phys. Rev. X* **8**, 041039 (2018).
- ³¹ J. M. Ni, Y. Y. Huang, E. J. Cheng, Y. J. Yu, B. L. Pan, Q. Li, L. M. Xu, Z. M. Tian, and S. Y. Li, *Nat. Commun.* **12**, 307 (2021).
- ³² R. Coldea, D. A. Tennant, E. M. Wheeler, E. Wawrzynska, D. Prabhakaran, M. Telling, K. Habicht, P. Smeibidl, and K. Kiefer, *Science* **327**, 177 (2010).
- ³³ Y. Shen, C. Liu, Y. Qin, S. Shen, Y. D. Li, R. Bewley, A. Schneidewind, G. Chen, and J. Zhao, *Nat. Commun.* **10**, 4530 (2019).
- ³⁴ Y. Cui, H. Zou, N. Xi, Z. He, Y. X. Yang, L. Shu, G. H. Zhang, Z. Hu, T. Chen, R. Yu, J. Wu, and W. Yu, *Phys. Rev. Lett.* **123**, 067203 (2019).
- ³⁵ C. Liu, C.-J. Huang, and G. Chen, *Phys. Rev. Research* **2**, 043013 (2020).
- ³⁶ H. Li, Y. D. Liao, B. B. Chen, X. T. Zeng, X. L. Sheng, Y. Qi, Z. Y. Meng, and W. Li, *Nat. Commun.* **11**, 1111 (2020).
- ³⁷ M. Inabayashi, Y. Doi, M. Wakeshima, and Y. Hinatsu, *Journal of the Ceramic Society of Japan* **126**, 920 (2018).
- ³⁸ A. Scheie, *J. Appl. Crystallogr.* **54**, 356 (2021).
- ³⁹ R. S. Hayano, Y. J. Uemura, J. Imazato, N. Nishida, T. Yamazaki, and R. Kubo, *Phys. Rev. B* **20**, 850 (1979).
- ⁴⁰ D. E. MacLaughlin, Y. Ohta, Y. Machida, S. Nakatsuji, G. M. Luke, K. Ishida, R. H. Heffner, L. Shu, and O. O. Bernal, *Physica B: Condensed Matter* **404**, 667 (2009).
- ⁴¹ G. Chen, *Phys. Rev. Research* **1**, 033141 (2019).